Chapter 4

ELECTRONIC STRUCTURES OF PERFUNCTIONALIZED DODECABORATE CLUSTERS

A manuscript based on the work presented in this chapter is being prepared for submission by Schwan, L. J.; Oyala, P. H.; Stauber. J. M.; Axtell, J. C. Winkler, J. R.; Spokoyny, A. M.; Gray, H. B. Electronic Structures of Perfunctionalized Dodecaborate Clusters.

Chapter 4 discusses our exploration of the electronic structures of hypoelectronic $[B_{12}(OR)_{12}]$ *clusters. Previous work has been focused on computational descriptions, as experimental investigations were hampered by the broad and unresolved continuous wave EPR spectra typically observed for open shell hypocloso-*$[B_{12}(OR)_{12}]^{1-}$ *species. Here, we use pulsed Q-band EPR techniques, with particular focus on ENDOR spectroscopy, to quantify the hyperfine interactions in these compounds and provide an experimental description of the SOMO(*a_{1u}*) spin density distribution. Furthermore, following our discovery of super-oxidized dodecaborate cations, we extended our pulsed EPR work to investigate the spin density distribution of the SOMO(*a_{2u}*) of* $[B_{12}(OR)_{12}]^{1+}$*. Our work convincingly shows that the frontier orbitals of* $[B_{12}(OR)_{12}]$ *clusters are confined to the cluster core and evenly delocalized across the 12 boron atoms. Comparisons between* $[B_{12}(OR)_{12}]^{1+}$ *cations and hypocloso-*$[B_{12}(OR)_{12}]^{1-}$ *anions further suggest that the spin density becomes more localized in more highly oxidized clusters. Besides our EPR investigations, we report UV–vis–NIR data which suggest that the visible and NIR transitions of hypoelectronic* $[B_{12}(OR)_{12}]$ *clusters involve orbitals largely confined to the cluster core. Ongoing work aims to produce a more comprehensive description of the electronic transitions through expansion of our UV–vis–NIR studies, and to perform in-depth analysis of the pulsed EPR data for the super-oxidized* $[B_{12}(OR)_{12}]^{1+}$ *clusters.*

4.1 Background

The discovery of a convenient process to perfunctionalize dodecaborate clusters, starting from dodecahydroxy-*closo*-dodecaborate (*closo*-$[B_{12}(OH)_{12}]^{2-}$), has led to the development of a range of aryloxy and alkyloxy-perfunctionalized dodecaborates ($[B_{12}(OR)_{12}]$; bracketing indicates an unspecified oxidation state if no oxidation number is given.).[1,2] While the parent *closo*-$[B_{12}H_{12}]^{2-}$ cluster is stable only in its dianionic closed-shell form,[3–7] the electron-donating OR groups allow $[B_{12}(OR)_{12}]$ to undergo two (aryl) or three (alkyl) reversible one-electron oxidations to form hypoelectronic *hypocloso*-$[B_{12}]^{1-}$ (25 electron), *hypercloso*-B_{12}^{0} (24 electron) and $[B_{12}]^{1+}$ (23 electron) cluster cores.[1,2,8] These clusters are promising candidates for a range of applications; recent examples include acting as combined photoinitiators and weakly coordinating proanions for cationic styrene polymerization[2,9], as well as for charge-storage devices[10] and as dopants in conducting polymers.[11] Here, we use pulsed electron paramagnetic resonance (EPR) techniques and UV-visible to near infrared (NIR) spectroscopies to investigate the electronic structure of five $[B_{12}(OR)_{12}]$ clusters: $[B_{12}(OCH_2C_6F_5)_{12}]$ ([**1**]), $[B_{12}(OCH_2(3,5\text{-}(CF_3)_2\text{-}C_6H_3)_{12}]$ ([**2**]), $[B_{12}(OBz)_{12}]$ ([**3**]), $[B_{12}(OEt)_{12}]$ ([**4**]). $[B_{12}(OC_2H_4{}^{i}Pr)_{12}]$ and ([**5**]) (Bz = $CH_2C_6H_5$, Et = C_2H_5, ^{i}Pr = C_3H_7).

The icosahedral *closo*-$[B_{12}H_{12}]^{2-}$ cluster is stabilized by a fully populated 4-fold degenerate B-B bonding HOMO(g_u) (highest occupied molecular orbital). Oxidation yields an unstable open shell species and leads to decomposition of the cluster.[3] However, some perfunctionalized dodecaborate clusters carrying electron-donating groups are able to accommodate hypoelectronic states. Examples include *hypocloso*-$[B_{12}(OR)_{12}]^{1-}$, *hypercloso*-$B_{12}(OR)_{12}$ (R = alkyl or aryl),[1,2,8,12,13] *hypocloso*-$[B_{12}Me_{12}]^{1-}$ (Me = CH_3)[14] and *hypocloso*-$[B_{12}X_{12}]^{1-}$ (X = F, Cl, Br, I).[15,16] Additionally, we recently discovered that $[B_{12}(OR)_{12}]$ clusters carrying certain alkyl substituents, such as [**4**] and [**5**], can accommodate a super-oxidized cationic $[B_{12}(OR)_{12}]^{1+}$ state (see Chapter 3).

Several factors contribute to the ability of $[B_{12}(OR)_{12}]$ clusters to support hypoelectronic oxidation states. Oxidized $[B_{12}H_{12}]$ species are not stable as depopulation of the four-fold degenerate B-B bonding HOMO(g_u) leads to an energetically unfavorable configuration. In hypoelectronic $[B_{12}(OR)_{12}]$ clusters, B-B bonding is enhanced through electron donation from the OR groups. Furthermore, structural distortion lowers the cluster core symmetry from I_h to D_{3d}, which splits the degenerate g_u set into orbitals of $a_{1u} + a_{2u} + e_u$ symmetry. Raising the depopulated SOMO(a_{1u}) (singly occupied molecular orbital; in $[B_{12}]^{1-}$) or LUMO(a_{1u}) (lowest unoccupied molecular orbital; in B_{12}^{0} and $[B_{12}]^{1+}$) and lowering of the fully populated HOMO-1(e_u) set (HOMO-1 refers to the second lowest energy occupied molecular orbital) reduces the overall energy of the cluster. Steric factors may also contribute to the stability of the cluster core, in particular when considering clusters carrying bulky fluoroaryl-substituents.[1,2,8,9,17,18] Motivated by the emerging applications and extraordinary ability to accommodate high oxidation states, we decided to perform an in-depth spectroscopic investigation of the electronic structures of $[B_{12}(OR)_{12}]$ clusters, hoping to provide comprehensive experimental descriptions of the frontier orbitals and electronic transitions of these clusters.

Attempts to examine the SOMO(a_{1u}) of monoanionic *hypocloso*-dodecaborate clusters using EPR spectroscopy have been restrained by the lack of resolution in continuous wave (CW) spectrum.[1,8,9,14] Even at high field strengths and low temperatures (285 GHz, 5 K) only very slight g-anisotropy is observed for $[B_{12}(OH)_{12}]^{1-}$.[17] It is generally believed that this is due to a highly delocalized SOMO, where the twelve near-equivalent boron nuclei give rise to a large number of overlapping hyperfine lines. This description has gained support from DFT calculations, although the details of the computational results vary significantly between different authors. We decided to investigate paramagnetic *hypocloso*-$[B_{12}(OR)_{12}]^{1-}$ and recently discovered $[B_{12}(OR)_{12}]^{1+}$ clusters using pulsed EPR techniques, hoping to verify the delocalized description of the frontier orbitals and show that the spin density is confined to the cluster core. To our knowledge this is the first time pulsed EPR data has been reported for paramagnetic dodecaborate clusters.

4.2 Pulsed EPR Investigation of *hypocloso*-$[B_{12}(OR)_{12}]^{1-}$

Q-band (34 GHz) EPR data was collected for the three anionic *hypocloso*-$[B_{12}(OR)_{12}]^{1-}$ clusters [**1**-**3**]$^{1-}$. [**1**]$^{1-}$ and [**2**]$^{1-}$ samples were prepared from their respective tetrabutylammonium (TBA) salts. Sufficiently pure salts of [**3**]$^{1-}$ have proven difficult to isolate, so we instead opted to prepare samples through *in-situ* reduction of **3**^{0} with triethylamine. As expected, Q-band Electron Spin Echo (ESE) EPR spectra of [**1**-**3**]$^{1-}$ show broad unresolved signals (Figure 4.1; g([**1**]$^{1-}$) = 2.00884, g([**2**]$^{1-}$) = 2.00883, g([**3**]$^{1-}$) = 2.00894), in line with reported X-band CW EPR spectra of *hypocloso*-$[B_{12}]^{1-}$ species. Davies Electron Nuclear Double Resonance (ENDOR) spectra for [**1**-**3**]$^{1-}$ are shown in Figure 4.2. The spectra were simulated as single class of rhombic $^{10/11}$B hyperfine couplings (|$A_{x,y,z}$([**1**]$^{1-}$)| = [0.1, 8.8, 12.9] MHz, |$A_{x,y,z}$([**2**]$^{1-}$)| = [0.1, 9.4, 13.1] MHz, |$A_{x,y,z}$([**3**]$^{1-}$)| = [0.1, 9.1, 12.6] MHz) and ^{1}H couplings (|$A_{x,y,z}$([**1**]$^{1-}$)| = [1, 9.5, 6] MHz, |$A_{x,y,z}$([**2**]$^{1-}$)| = [1, 9.5, 6] MHz, |$A_{x,y,z}$([**3**]$^{1-}$)| = [1, 10, 6] MHz). g-values and hyperfine tensors are compared in Table 4.1. The simulations were refined using the Mims ENDOR spectra shown in Figure 4.3 and HYSCORE data. Figure 4.4 shows the [**3**]$^{1-}$ HYSCORE along with the results from simulations using the hyperfine tensors above. In addition to what can be observed in the Davies ENDOR, the Mims ENDOR spectra indicated a class of very weak hyperfine couplings to ^{19}F ($|A_{x,y,z}| < 0.5$Mhz) for both **[1]**$^{1-}$ and **[2]**$^{1-}$.

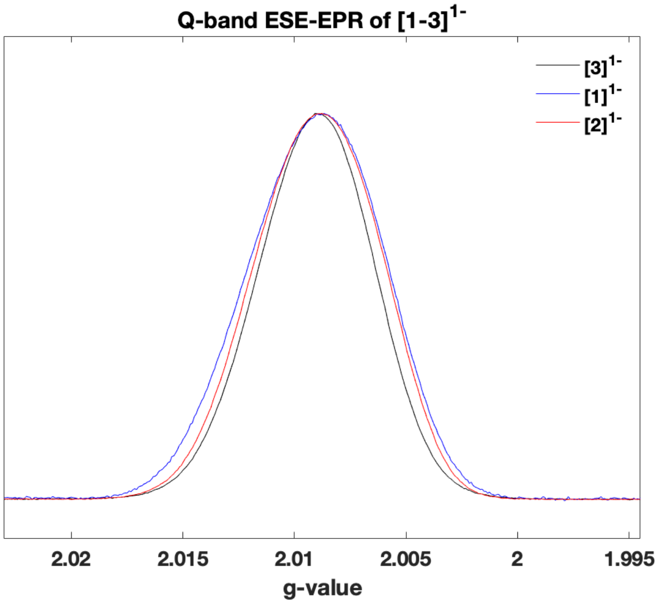

Figure 4.1. Q-band ESE-EPR spectra of [**1**-**3**]$^{1-}$ collected at 5 K and 34.11 GHz microwave frequency. Fitting of the ESE-EPR data yields isotropic g-values: g([**1**]$^{1-}$) = 2.00884, g([**2**]$^{1-}$) = 2.00883, g([**3**]$^{1-}$) = 2.00894.

The hyperfine coupling tensors are near identical between the three clusters, indicating a cluster core confined SOMO(a_{1u}) where the R-groups do not significantly perturb the spin density distribution. The very weak ^{19}F hyperfine coupling, which likely stems from through-space interactions, further substantiate a cluster core confined description. That we only observe a single class of $^{10/11}$B hyperfine interactions strongly supports describing the SOMO(a_{1u}) as evenly delocalized over twelve near-equivalent boron nuclei. Calculating quantitative spin densities remains a major challenge as it requires determining the relative orientation of all the contributing boron 2p orbitals. In this chapter, we have limited our quantitative calculations to the s-orbital spin densities, which can be readily obtained from the isotropic component of the hyperfine tensor. These calculations (see Section 4.6 for details) give a total boron 2s orbital spin density of ρ_{2s} = 3.4% (~0.3% on each of the 12 boron nuclei). Analogous calculations for the 24 proton 1s orbitals yield a total orbital spin density of ρ_{1s} = 9.9%. Rather than considering a SOMO(a_{1u}) extended beyond the oxygens, which would be inconsistent with the very weak ^{19}F hyperfine coupling, we believe the ^{1}H hyperfine interactions stem from hyperconjugation between β-protons and oxygen 2p spin density.

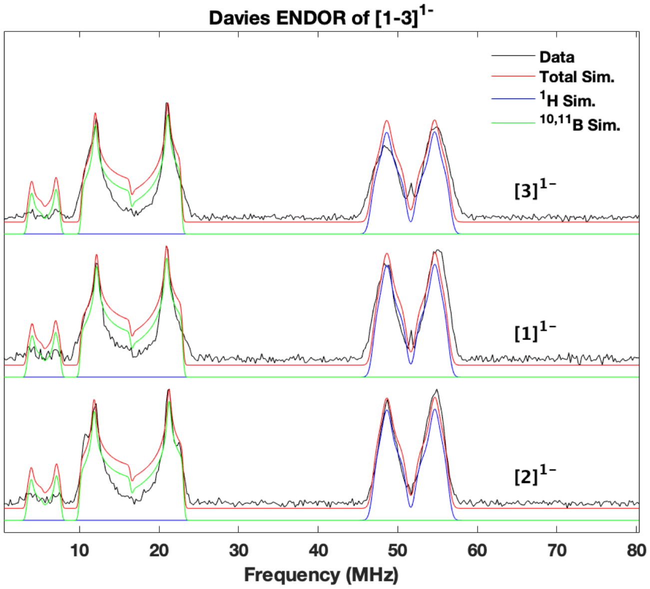

Figure 4.2. Davies ENDOR spectra of [**1**-**3**]$^{1-}$ collected at 5 K and 34.11 GHz microwave frequency. The colored lines show results from simulations using g([**1**]$^{1-}$) = 2.00884, g([**2**]$^{1-}$) = 2.00883, g([**3**]$^{1-}$) = 2.00894, and $^{10/11}$B hyperfine tensors $|A_{x,y,z}$([**1**]$^{1-}$)$|$ = [0.1, 8.8, 12.9] MHz, $|A_{x,y,z}$([**2**]$^{1-}$)$|$ = [0.1, 9.4, 13.1] MHz and $|A_{x,y,z}$([**3**]$^{1-}$)$|$ = [0.1, 9.1, 12.6] MHz, and ^{1}H hyperfine tensors $|A_{x,y,z}$([**1**]$^{1-}$)$|$ = [1, 9.5, 6] MHz, $|A_{x,y,z}$([**2**]$^{1-}$)$|$ = [1, 9.5, 6] MHz, $|A_{x,y,z}$([**3**]$^{1-}$)$|$ = [1, 10, 6] MHz. Blue lines represent the ^{1}H simulation, green lines the $^{10/11}$B simulation and red lines the total simulation combining both ^{1}H and $^{10/11}$B contributions.

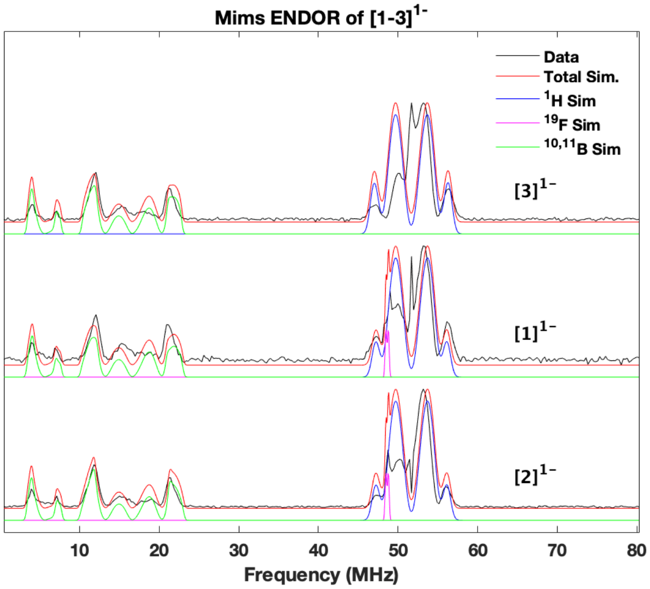

Figure 4.3. Mims ENDOR spectra of [**1**-**3**]$^{1-}$ collected at 5 K and 34.11 GHz microwave frequency. A very weak ^{19}F hyperfine coupling can be observed on the left side of the ^{1}H signal. The colored lines show results from simulations using g([**1**]$^{1-}$) = 2.00884, g([**2**]$^{1-}$) = 2.00883, g([**3**]$^{1-}$) = 2.00894, and the ^{19}F hyperfine tensor $A_{x,y,z}$ = [-0.25 0.5 -0.25] MHz, $^{10/11}$B hyperfine tensors $|A_{x,y,z}$([**1**]$^{1-}$)$|$ = [0.1, 8.8, 12.9] MHz, $|A_{x,y,z}$([**2**]$^{1-}$)$|$ = [0.1, 9.4, 13.1] MHz and $|A_{x,y,z}$([**3**]$^{1-}$)$|$ = [0.1, 9.1, 12.6] MHz, and ^{1}H hyperfine tensors $|A_{x,y,z}$([**1**]$^{1-}$)$|$ = [1, 9.5, 6] MHz, $|A_{x,y,z}$([**2**]$^{1-}$)$|$ = [1, 9.5, 6] MHz, $|A_{x,y,z}$([**3**]$^{1-}$)$|$ = [1, 10, 6] MHz. Blue lines represent the ^{1}H simulation, green lines the $^{10/11}$B simulation and red lines the total simulation combining both ^{1}H and $^{10/11}$B contributions.

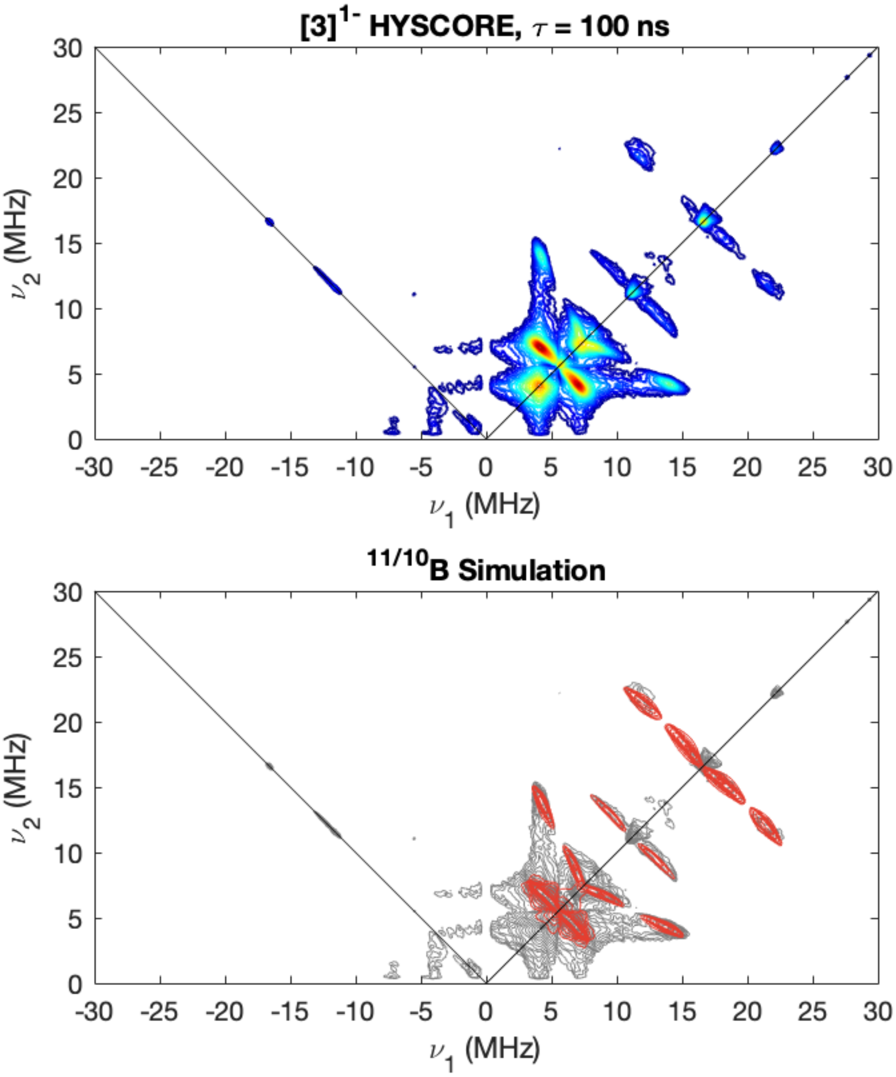

Figure 4.4. The top image shows HYSCORE data for [**3**]$^{1-}$ collected at 50 K and 34.11 GHz microwave frequency. Results for [**1**]$^{1-}$ and [**2**]$^{1-}$ are similar to the data presented here. The image figure shows the $^{10/11}$B simulation (red) obtained using g([**3**]$^{1-}$) = 2.00894 and a $|A_{x,y,z}$([**3**]$^{1-}$)$|$ = [0.1, 9.1, 12.6] MHz hyperfine tensor. The underlying gray contour map corresponds to the experimental data.

4.3 Pulsed EPR Investigation of Super-Oxidized $[B_{12}(OR)_{12}]^{1+}$ Clusters

Motivated by our successful application of pulsed EPR techniques to the *hypocloso*-$[B_{12}(OR)_{12}]^{1-}$ clusters, we decided to explore the recently discovered super-oxidized $[B_{12}(OR)_{12}]^{1+}$ cation. Samples of [**4**-**5**]$^{1+}$ were prepared through *in-situ* oxidation of **4**^{0} and **5**^{0} using a substochiometric amount of the strong oxidant tris(2,4-dibromophenyl)ammoniumyl hexachloroantimonate. Interestingly, the Q-band ESE-EPR spectrum, shown in Figure 4.5, of these species display some anisotropy in the g-tensor ($g_{x,y,z}$([**5**]$^{1+}$) = [2.0140 2.0082 2.0002]). This suggests that the cluster core is more distorted than in the [**1**-**3**]$^{1-}$ anions, which is not surprising given that further splitting the HOMO-1(e_u) set and the SOMO(a_{2u}) would likely result in a more stable cluster core. Figure 4.6 demonstrates the resemblance of the Davies ENDOR for [**4**-**5**]$^{1+}$ and [**3**]$^{1-}$, indicating that the SOMO distribution is similar in both the anion and the cation. Figure 4.7 and 4.8 shows simulations of the Davies ENDOR spectra and HYSCORE of [**5**]$^{1+}$, using hyperfine tensors relatively similar to those observed for [**1**-**3**]$^{1-}$ ($^{10/11}$B $|A_{x,y,z}$([**5**]$^{1+}$)$|$ = [0.1 8.5 13.5] MHz and ^{1}H $|A_{x,y,z}$([**5**]$^{1+}$)$|$ = [0.5 11 7] MHz). Interestingly, the HYSCORE of [**4**]$^{1+}$, for which we were able to obtain a significantly improved signal-to-noise, indicate that an additional class of weak ^{11}B hyperfine interactions are present (Figure 4.9). We are at this time unsure whether this weak signal indicates that [**4**]$^{1+}$ is more distorted than [**5**]$^{1+}$, or if we are simply not resolving the analogous features for [**5**]$^{1+}$ due to poor signal intensity. Figure 4.10 compares Davies ENDOR spectra of [**4**]$^{1+}$ at the high and low field edges. At the low field edge, the $^{10/11}$B signal appear broadened beyond detection, which is not suspiring given the broadness of the HYSCORE features in that quadrant. Simulations of the [**4**]$^{1+}$ data are currently underway.

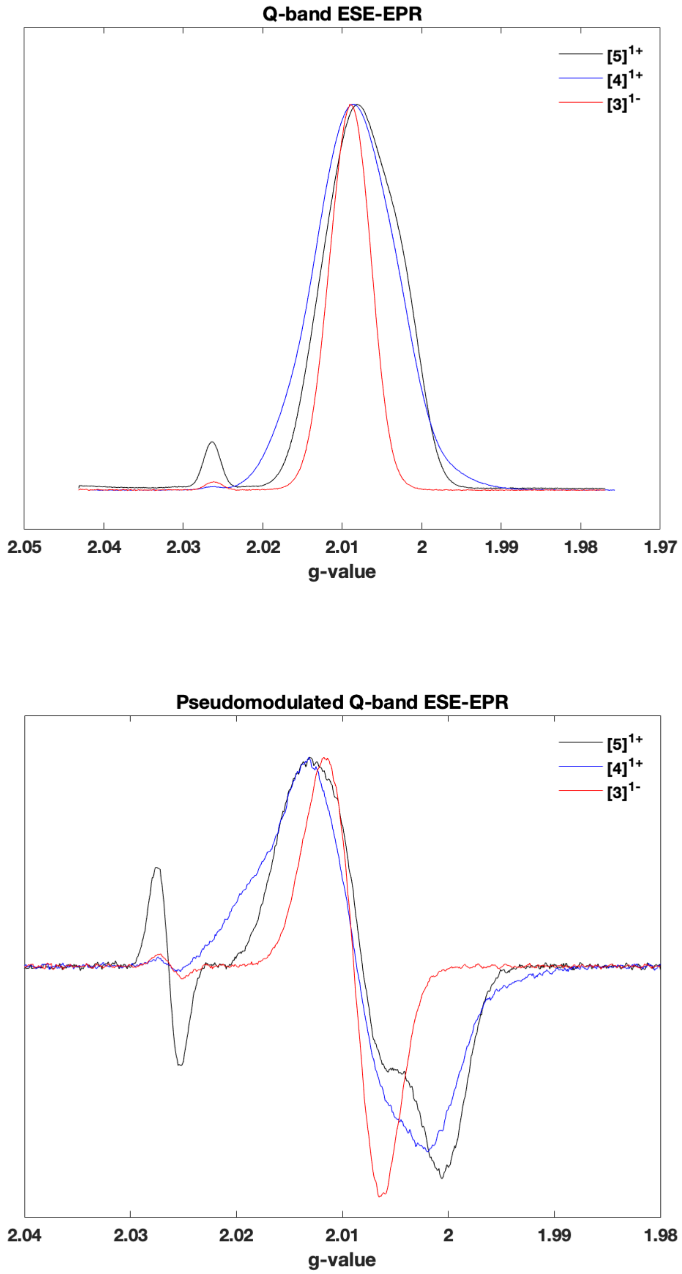

Figure 4.5. (Top) ESE-EPR spectra and (Bottom) pseudomodulated ESE-EPR spectra for [**4**-**5**]$^{1+}$ collected 32 K and 34.11 GHz ([**5**]$^{1+}$) or 34.13 GHz ([**4**]$^{1+}$) microwave frequency. Data for [**3**]$^{1-}$ is shown for comparison, demonstrating the significantly increased g-anisotropy. [**3**]$^{1-}$ data was collected at 5 K and 34.11 GHz microwave frequency. Fitting of the [**5**]$^{1+}$ ESE-EPR spectrum gives $g_{x,y,z}$([**5**]$^{1+}$) = [2.0140 2.0082 2.0002].

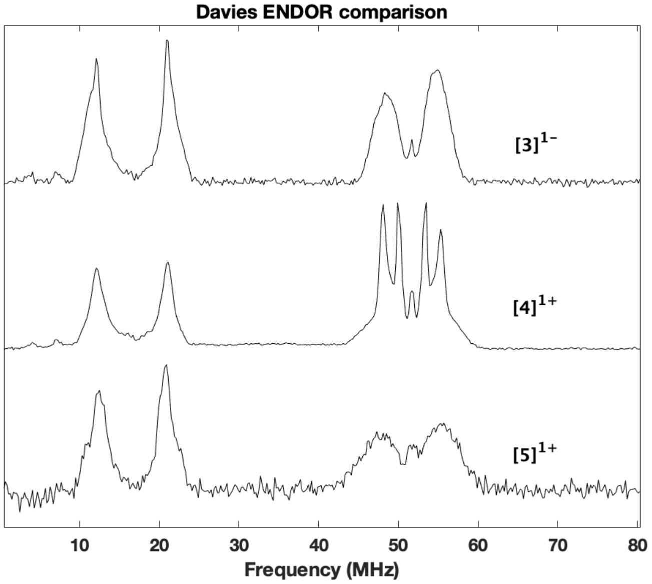

Figure 4.6. Davies ENDOR spectra for [**4**-**5**]$^{1+}$ compared to a spectrum collected for [**3**]$^{1+}$, demonstrating the similarities between the anion and cation data. Data was collected at 5 K ([**3**]$^{1-}$), 25 K ([**4**]$^{1+}$) and 18 K ([**3**]$^{1+}$). Microwave frequencies were the same as used for the ESE-EPR data (see Figure 4.5).

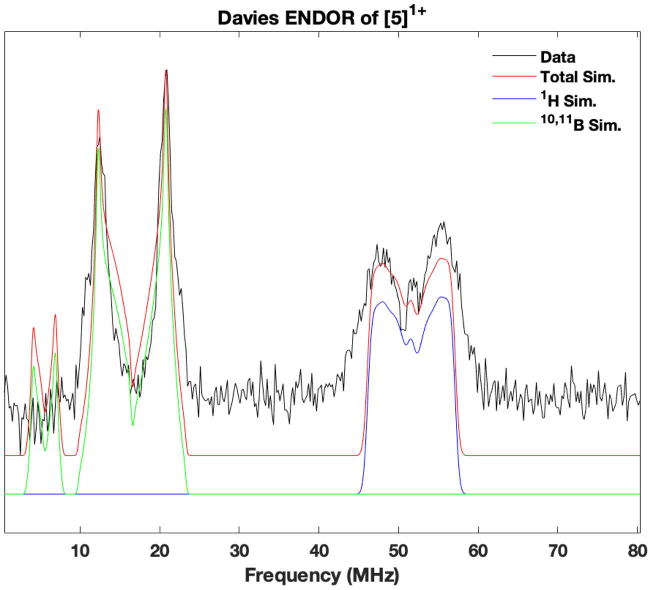

Figure 4.7. The black line shows the Davies ENDOR data for [**5**]$^{1+}$. The colored lines show simulations to $g_{x,y,z}$ = [2.0140 2.0082 2.0002] $^{10/11}$B $|A_{x,y,z}|$ = [0.1, 8.5, 13.5] MHz and ^{1}H $|A_{x,y,z}|$ = [0.5 11 7] MHz. Blue lines represent the ^{1}H simulation, green lines the $^{10/11}$B simulation and red lines the total simulation combining both ^{1}H and $^{10/11}$B contributions.

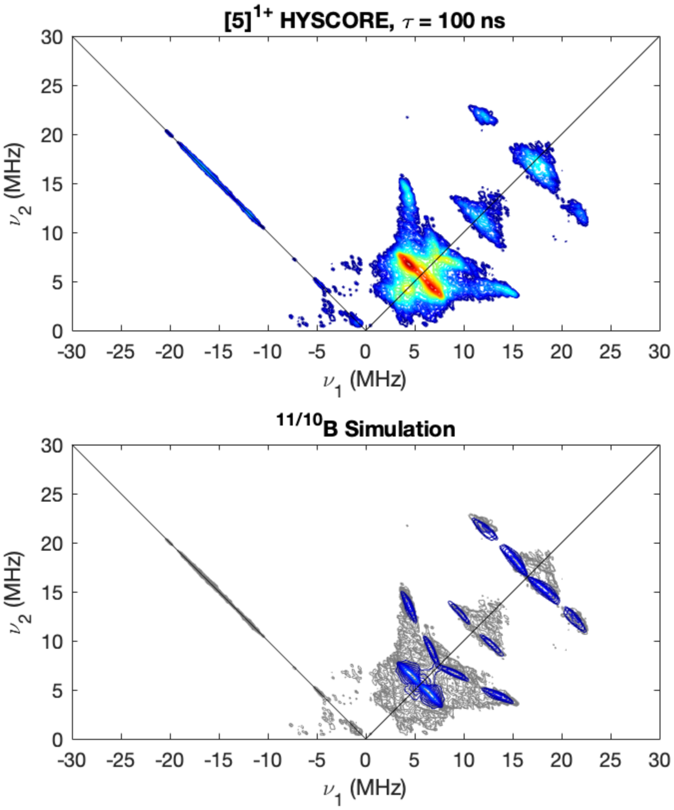

Figure 4.8. (Top) [**5**]$^{1+}$ HYSCORE collected at 32 K and 34.11 GHz microwave frequency. (Bottom) HYSCORE data in gray and simulation to $g_{x,y,z}$ = [2.0140 2.0082 2.0002] and $|A_{x,y,z}|$ = [0.1, 8.5, 13.5] MHz in color.

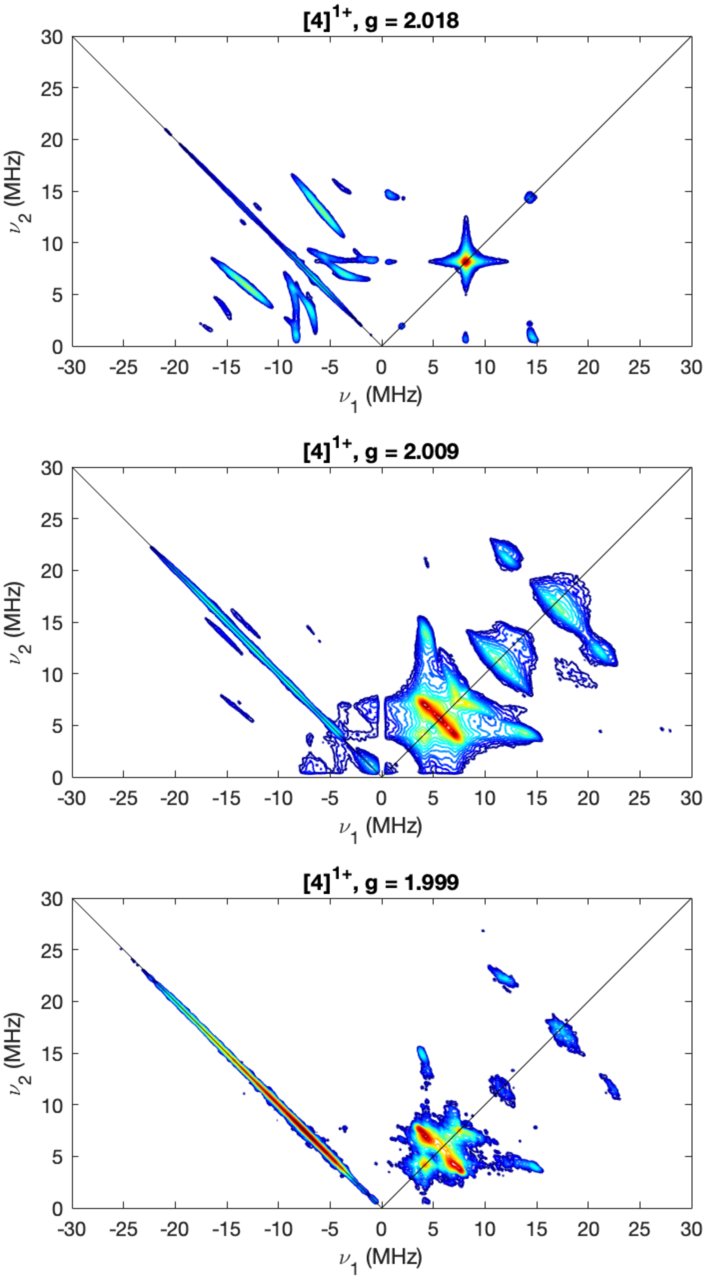

Figure 4.9. HYSCORE data collected for [**4**]$^{1+}$ at 25 K and 34.13 GHz microwave frequency. A broad feature appears in the left quadrant at the low field edge.

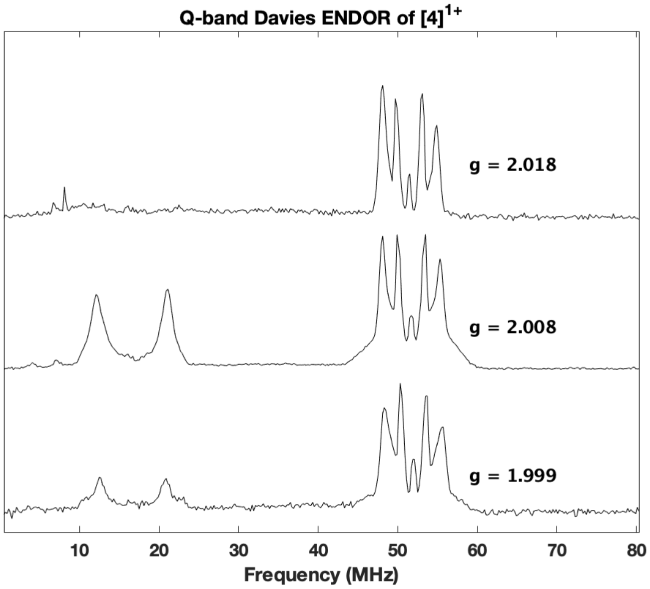

Figure 4.10. Comparison of Davies ENDOR spectra of [**4**]$^{1+}$ at the low field edge, mid field and high field edge. Data was collected at 25 K and 34.13 GHz microwave frequency. Analogous data collected for [**1**-**3**]$^{1-}$ do not show significant field dependence (see Section 4.6).

The mid field ENDOR spectra of [**4**-**5**]$^{1+}$ are comparable to spectra collected for the [**1**-**3**]$^{1-}$ anions, suggesting that the distribution of the SOMO(a_{2u}) is similar to the SOMO(a_{1u}) of the anions. This is further validated by the likeness of the simulated hyperfine tensors of [**5**]$^{1+}$ compared to [**1**-**3**]$^{1-}$. This is expected, as the SOMO (a_{1u} symmetry in $[B_{12}]^{1-}$ and a_{2u} symmetry in $[B_{12}]^{1+}$) stem from the same degenerate I_h symmetry HOMO(g_u) in both cases. However, the anisotropy in the ESE-EPR indicates that the SOMO(a_{2u}) is not equally distributed across all twelve boron nuclei. This is further supported by the ENDOR field dependence and the additional features in the HYSCORE of [**4**]$^{1+}$. This could be due to inherent differences in the orbital geometry between aryl-functionalized and alkyl-functionalized clusters, but a more probable cause is increased distortion in the cluster core of the more oxidized species. Although we have not yet been able to structurally characterize any super-oxidized $[B_{12}(OR)_{12})]^{1+}$ clusters, we postulate that the cluster core is elongated along the z-axis, resulting in a SOMO(a_{2u}) with the majority of the spin density centered around the equatorial belt. g-values and hyperfine tensors obtained for [**1**-**3**]$^{1-}$ and [**5**]$^{1+}$ are summarized in Table 4.1.

Table 4.1. g-values and hyperfine tensors obtained by simulation of ESE-EPR, ENDOR and HYSCORE data.

	$g_{x,y,z}$	**^{1}H |$A_{x,y,z}$| (MHz)**	**$^{10/11}$B |$A_{x,y,z}$| (MHz)**	**^{19}F |$A_{x,y,z}$| (MHz)**
[**1**]$^{1-}$	2.00884	[1 9.5 6]	[0.1 8.8 12.9]	< 0.5
[**2**]$^{1-}$	2.00883	[1 9.5 6]	[0.1 9.4 13.1]	< 0.5
[**3**]$^{1-}$	2.00894	[1 10 6]	[0.1 9.1 12.6]	-
[**5**]$^{1+}$	[2.0140 2.0082 2.0002]	[0.5 11 7]	[0.1 8.5 13.5]	-

4.4 Electronic Transitions in $[B_{12}(OR)_{12}]$ Clusters

UV–vis–NIR spectra of $\mathbf{1}^0$, $\mathbf{2}^0$, TBA[**1**] and TBA[**2**] are shown Figure 4.11 and 4.12, while spectra of the alkyloxy functionalized clusters are shown in Figure 4.13 ($\mathbf{4}^0$ and $\mathbf{5}^0$) and 4.14 ($[\mathbf{4}]^{1+}$). The excitation energies and extinction coefficients are summarized in Table 4.2. The dianionic *closo*-$[B_{12}(OR)_{12}]^{2-}$ clusters are colorless, consistent with the large energy gap expected between the four-fold degenerate HOMO(g_u) and LUMO(g_g).[18] Depopulation of the HOMO gives rise to a strong visible absorption band (ES3). In the anionic TBA[**1**] and TBA[**2**] cluster ES3 appears around 525 nm ($1.9*10^5$ cm^{-1}, ~$1.5*10^4$ M^{-1} cm^{-1}), while in the neutral $\mathbf{1}^0$ and $\mathbf{2}^0$ clusters it is blue-shifted to around 455 nm ($2.2*10^5$ cm^{-1}, ~$3*10^4$ M^{-1} cm^{-1}). The alkyloxy-perfunctionalized $\mathbf{4}^0$ and $\mathbf{5}^0$ clusters show analogous absorption bands blue-shifted by 5-10 nm. Given that the energy of

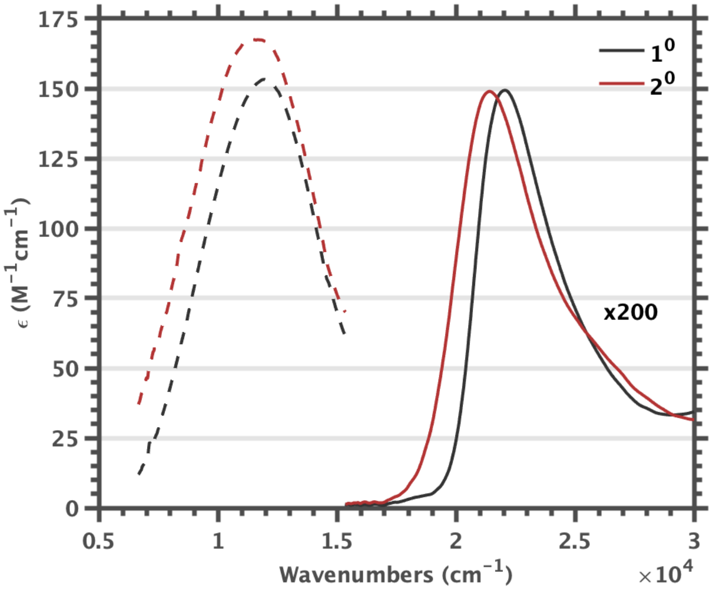

Figure 4.11. UV–vis–NIR spectra of $\mathbf{1}^0$ and $\mathbf{2}^0$ collected in dichloromethane-d_2. The visible band is displayed at approximately 1/200 of its actual extinction coefficient.

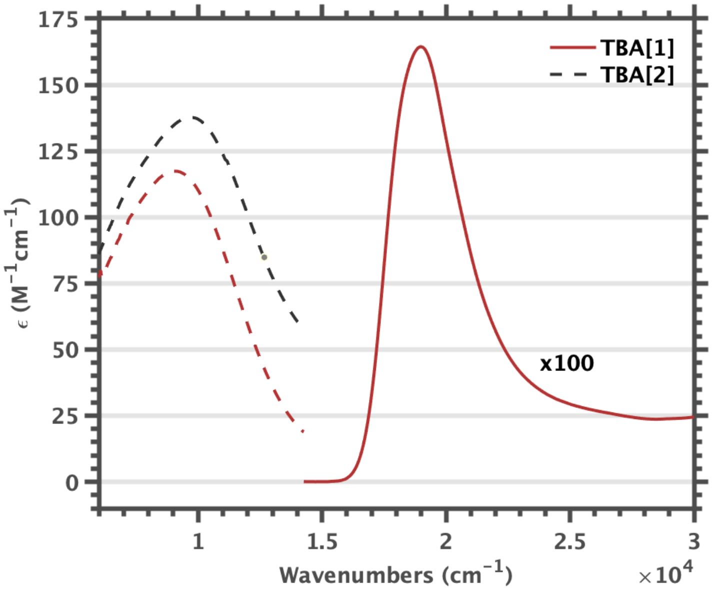

Figure 4.12. UV–vis–NIR spectra of TBA[**1**] and TBA[**2**] collected in dichloromethane-*d*$_2$. The visible band is displayed at approximately 1/100 of its actual extinction coefficient.

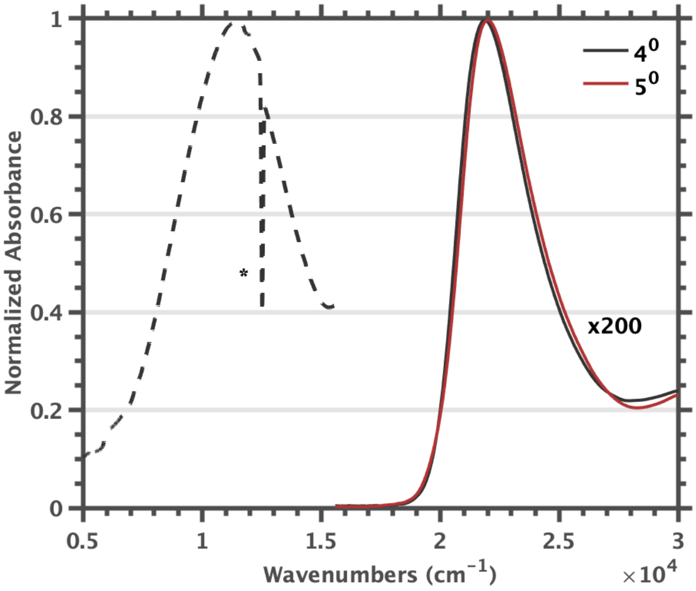

Figure 4.13. UV–vis–NIR spectra of **4**^{0} and **5**^{0} collected in dichloromethane-*d*$_2$. The visible band is displayed at approximately 1/100 of its actual intensity. Extinction coefficients are comparable to **1**^{0}-**2**^{0}.

ES3 is largely independent of R-group, we believe this transition must occur between cluster core-based orbitals. Most likely, the donor orbital stems from the five-fold degenerate I_h HOMO-1(h_g), which splits into one a_{1g} symmetry and two sets of e_g symmetry orbitals upon distortion to D_{3d}. The ground state of the closed-shell *hypercloso*-$B_{12}(OR)_{12}$ species is $^1A_{1g}$. Transitions from orbitals of a_{1g} or e_g symmetry would yield $^1A_{1u}$ or ^1E_u excited states. Orbital selection rules state that electronic transitions are allowed if and only if equation 4.1 contains the fully symmetric representation (a_{1g}).

$$\Gamma(\psi_e^*) \times \Gamma(\hat{\mu}_e) \times \Gamma(\psi_e) \tag{4.1}$$

where ψ_e^* is the excited-state wavefunction, ψ_e is the ground state wave function and $\hat{\mu}_e$ is the dipole moment operator ($\begin{pmatrix} a_{2u} \\ e_u \end{pmatrix}$ in D_{3d}).[19] Examining the excited states above, we get the expressions show in equations 4.2 and 4.3.

$$A_{1u} \leftarrow A_{1g}: A_{1u}\begin{pmatrix} a_{2u} \\ e_u \end{pmatrix} A_{1g} = \begin{pmatrix} a_{2g} \\ e_g \end{pmatrix} \tag{4.2}$$

$$E_u \leftarrow A_{1g}: E_u\begin{pmatrix} a_{2u} \\ e_u \end{pmatrix} A_{1g} = \begin{pmatrix} e_g \\ \boldsymbol{a_{1g}} + a_{2g} + e_g \end{pmatrix} \tag{4.3}$$

From these considerations, it becomes clear that only the $^1E_u \leftarrow {}^1A_{1g}$ transition is allowed. The high extinction coefficient of ES3 strongly suggests that it corresponds to this transition. Analogous considerations can be used to show that the ~525 nm ES3 in open-shell *hypocloso*-$[B_{12}(OR)_{12}]^{1-}$ clusters correspond to an $^2E_g \leftarrow {}^2A_{1u}$ transition.

Both neutral *hypercloso*-$B_{12}(OR)_{12}$ and anionic *hypocloso*-$[B_{12}(OR)_{12}]^{1-}$ clusters display weak NIR bands with extinction coefficients around 150 $M^{-1}cm^{-1}$ (ES1). These bands are shown along with the visible spectra in Figures 4.11–4.13. We suggest ES1 correspond to symmetry forbidden transitions between orbitals of g_u parentage, e.g. $^1A_{2g}\leftarrow{}^1A_{1g}$ or $^1E_g\leftarrow{}^1A_{1g}$ for *hypercloso*-$B_{12}(OR)_{12}$ and $^2A_{2u}\leftarrow{}^2A_{1u}$ or $^2E_u\leftarrow{}^2A_{2u}$ for *hypocloso*-$[B_{12}(OR)_{12}]$. Although we feel confident in our assignments, we cannot definitively say that ES1 does not involve orbitals with more ligand character, for example lone pairs on the oxygens.

Oxidation of $\mathbf{4}^0$ to the super-oxidized $[\mathbf{4}]^{1+}$ species slightly blue-shifts ES3 and gives rise to a new absorption band centered at 706 nm (ES2). In $[\mathbf{4}]^{1+}$ both the LUMO(a_{1u}) and SOMO(a_{2u}) can act as acceptor orbitals, which likely explain the appearance of the new absorption band. Similar to ES3, we suggest the donor orbital(s) in ES2 are of I_h HOMO-1(h_g) parentage. Forbidden lower-energy transitions analogous to ES1 are likely also accessible in $[B_{12}(OR)_{12}]^{1+}$ clusters, however, we have so far been unable to collect NIR spectra of $[\mathbf{4}]^{1+}$ and $[\mathbf{5}]^{1+}$ due to in-solution stability issues. Following the selection rule arguments discussed above, ES3 in $[B_{12}(OR)_{12}]^{1+}$ is likely an $^2E_g\leftarrow{}^2A_{2u}$ transition involving the same e_g symmetry donor orbitals as ES3 in *hypercloso*-$B_{12}(OR)_{12}$ and *hypocloso*-$[B_{12}(OR)_{12}]^{1-}$. The energy difference between ES2 and ES3 is Δ(ES3-ES2) ≈ 8000 cm^{-1}. It is interesting to compare this value to the ES1 energy, as both provide indications of the energy splitting between the LUMO(a_{1u}), SOMO(a_{2u}) and HOMO-1(e_u) orbitals. Given that the ES1 energy appears to increase as the clusters become more oxidized, we presume that the ES1 energy of $[\mathbf{4}]^{1+}$ is similar or larger than the ES1 energy of $\mathbf{4}^0$ (11500 cm^{-1}). This means that ES1 is at least 2500 cm^{-1} higher than Δ(ES3-ES2), which could indicate that the ES1 donor orbital is the HOMO-1(e_g) set, rather than the SOMO-1(a_{2u}). For ES2 eq. 4.4 and 4.5 show that transitions from orbitals of both a_{1g} and e_g symmetry could be allowed, assuming the SOMO(a_{2u}) is the acceptor orbital, which further complicates the analysis.

$$A_{1g} \leftarrow A_{2u}: A_{1g}\binom{a_{2u}}{e_u}A_{2u} = \binom{\boldsymbol{a_{1g}}}{e_g} \tag{4.4}$$

$$E_g \leftarrow A_{2u}: E_g\binom{a_{2u}}{e_u}A_{2u} = \binom{e_g}{\boldsymbol{a_{1g}}+a_{2g}+e_g} \tag{4.5}$$

Future spectroscopic work investigating NIR transitions in $[B_{12}(OR)_{12}]^{1+}$ may shed more light on the identity of these transitions.

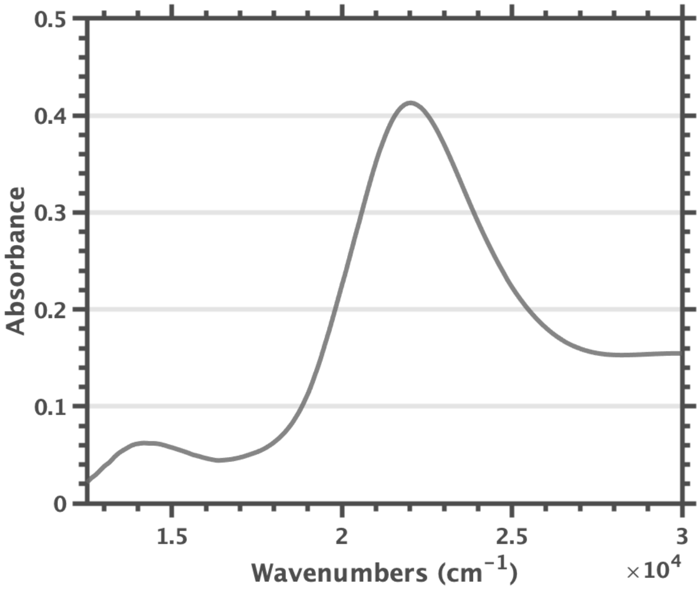

Figure 4.14. Electrochemically generated visible spectrum of [**4**]$^{1+}$ collected in 0.1 M tetrabutylammonium hexafluorophosphate dichloromethane electrolyte. Experimental details can be found in Chapter 3.

Table 4.2. Excitation energies and extinction coefficients (ε) obtained from UV–vis–NIR spectra. *k* is the excitation energy in cm-1, while λ is the excitation energy in $M^{-1}cm^{-1}$. ES1 is the lowest energy excited state, ES2 the second lowest energy excited state and ES3 the third lowest energy excited state (not considering triplets). ES2 is only observed in the $[\mathbf{4}]^{1+}$ cation. We expect ES1 to be accessible in $[\mathbf{4}]^{1+}$ but have so far not been able to experimentally observe it.

	ES1		**ES2**		**ES3**	
	k **(cm^{-1}) [λ (nm)]**	**ε ($M^{-1}cm^{-1}$)**	***k*** **(cm^{-1}) [λ (nm)]**	**ε ($M^{-1}cm^{-1}$)**	***k*** **(cm^{-1}) [λ (nm)]**	**ε ($M^{-1}cm^{-1}$)**
$[\mathbf{1}]^{1-}$	$9.69*10^3$ [1030]	140	-	-	$2.20*10^4$ [455]	$1.5*10^4$
$\mathbf{1}^0$	$1.20*10^4$ [837]	150	-	-	$2.21*10^4$ [453]	$2.9*10^4$
$[\mathbf{2}]^{1-}$	$9.06*10^3$ [1100]	120	-	-	$1.90*10^4$ [527]	$1.6*10^4$
$\mathbf{2}^0$	$1.14*10^4$ [875]	170	-	-	$2.18*10^4$ [457]	$2.9*10^4$
$\mathbf{4}^0$	$1.15*10^4$ [871]	~150	-	-	$2.19*10^4$ [457]	$3*10^4$
$[\mathbf{4}]^{1+}$	?	?	$1.42*10^4$ [706]	$\sim 5*10^3$	$2.20*10^4$ [454]	$\sim 2.5*10^4$
$\mathbf{5}^0$	?	?	-	-	$2.20*10^4$ [454]	$3*10^4$

4.5. Conclusions

The pulsed EPR work presented here provides strong experimental evidence supporting a cluster-confined but highly delocalized description of the $[B_{12}(OR)_{12}]$ frontier orbitals. In addition to offering an experimental description of the spin density, we suggest that the hyperfine tensors obtained from our simulations can help guide and improve the accuracy future computational studies. Furthermore, we hope other researcher will be inspired to apply similar methods to study the frontier orbitals of other hypoelectronic dodecaborates clusters such as *hypocloso*-$[B_{12}X_{12}]^{1-}$ and *hypocloso*-$[B_{12}Me_{12}]^{1-}$.

The NIR and visible absorption bands of $[B_{12}(OR)_{12}]$ clusters are best described as transitions between orbitals primarily confined to the cluster core. This is most evident for ES3, where the excitation energy is nearly independent of the R substituent. Additional work is required to definitively assign the transitions. Two key areas include obtaining NIR spectra of super-oxidized $[B_{12}(OR)_{12}]^{1+}$ clusters, which would provide further evidence of transitions between orbitals of I_h symmetry g_u parentage, and calculating of $E_{0,0}$ energies from emission spectra.

4.6 Experimental Details

Compounds

1^0-**5**^{0}, [TBA][**1**] and [TBA][**2**] were kindly gifted by the Spokoyny lab. We did not attempt study [**4**-**5**]$^{1-}$ as these species appear to disproportionate in solution.

Electron Paramagnetic Resonance

Sample preparation

All samples were prepared in quartz Q-band EPR tubes (Wilmad WG-221T-RB), ID = 1.1 mm, OD = 1.6 mm, L = 10 cm. A nitrogen-filled glove box was used for generation and manipulation of [**4**-**5**]$^{1+}$. Toluene (Millipore) had been dried on a commercial solvent purification system and further degassed through at least three freeze-pump-thaw cycles before introduction to the glove box. Inside the glove box, the solvent was stored over activated 3 Å molecular sieves (Sigma-Aldrich). Perfluorotoluene (TCI) and perfluoro-methylcyclohexane (TCI) were dried over 3 Å molecular sieves for > 84 hours, followed by distillation, discarding the initial and final fractions. Anhydrous diochloromethane-d_2 (Cambridge Isotope Labs) was used as received. Before use, the solvents were degassed by at least three freeze-pump-thaw cycles. Tris(2,4-dibromophenyl)ammoniumyl hexachloroantimonate was obtained from the Spokoyny lab.

[**1**]$^{1-}$: Sample prepared using standard air-free techniques. 8 mg of [TBA][**1**] was dissolved in 0.2 ml toluene. The solution was then diluted to 2 ml and transferred to a Q-band EPR tube. The sample was immediately frozen in liquid nitrogen.

[**2**]$^{1-}$: Sample prepared using standard air-free techniques. [TBA][**2**] was dissolved in 5:1 perfluorotoluene/perfluoro-methylcyclohexane and transferred to a Q-band EPR tube. The sample was immediately frozen in liquid nitrogen.

[**3**]$^{1-}$: Sample prepared open-air. 3 mg of **3**^{0} was added to 2 ml 1 mM triethylamine toluene solution. The sample was transferred to a Q-band EPR tube and immediately frozen in liquid nitrogen.

[**4**]$^{1+}$: Sample prepared inside a nitrogen-filled glove box. 4.5 mg tris(2,4-dibromophenyl)ammoniumyl hexachloroantimonate and 3.4 mg **4**^{0} was dissolved in a toluene/dichloromethane-d_2 mixture (1 ml toluene, 1 g dichloromethane-d_2). The solution was mixed until all of the oxidant had been consumed (determined visually). The sample was immediately transferred to a Q-band EPR tube and frozen in liquid nitrogen. The frozen sample was handled under ambient conditions, taking care not to thaw the solution.

[**5**]$^{1+}$: Sample prepared inside a nitrogen-filled glove box. 1.7 mg tris(2,4-dibromophenyl)ammoniumyl hexachloroantimonate and 3 mg **5**^{0} was dissolved in 1 ml toluene. The solution was mixed until all of the oxidant had been consumed (determined visually). The sample was immediately transferred to a Q-band EPR tube and frozen in liquid nitrogen. The frozen sample was handled under ambient conditions, taking care not to thaw the solution.

Pulsed EPR experiments

All pulsed EPR spectra were obtained on a Bruker (Billerica, MA) ELEXSYS E580 pulse EPR spectrometer equipped with a Bruker D2 ENDOR resonator and an ER 4118HV-CF5-L Flexline Cryogen-Free VT cryostat (ColdEdge, Allentown, PA) combined with an Oxford Instruments Mercury ITC. Descriptions of the ESE-EPR, Davies ENDOR, Mims ENDOR and HYSCORE experiments can be found in the literature.[20–27]

Simulation

MATLAB R2019a (MathWorks) was used along with the EasySpin[25] software package to simulate pulsed EPR data. ESE-EPR spectra were fitted using the Pepper function. ENDOR spectra were simulated using the Salt function and g-values from the ESE-EPR fitting. HYSCORE data was used to refine hyperfine tensors by simulation using the Saffron function.

Spin density calculations

The observed hyperfine tensors (**A**), contains both isotropic and anisotropic contributions. The mean of the hyperfine tensor corresponds to the isotropic contributions (a_{iso}). Subtracting a_{iso} from **A** yields the anisotropic contributions ($\boldsymbol{A}_{aniso}$). Considering the ^{11}B hyperfine tensor of [**1**]$^{1-}$ as an example:

$$\mathbf{A}\left(^{11}B\right) = [0.1\ 8.8\ 12.9]\ \text{MHz} = a_{iso} + \boldsymbol{A}_{aniso} = 7.3 + [-7.2\ 1.5\ 5.6]\ \text{MHz} \tag{4.6}$$

The s-orbital spin density can be readily calculated by dividing a_{iso} with the calculated isotropic hyperfine interaction for unit spin density (a_{iso}^{0}).[28] The anisotropic part of the hyperfine tensor represents contributions from non-spherical orbitals (p, d, f). To estimate spin densities from the anisotropic hyperfine, the isotropic hyperfine parameter (P) has to be considered along with an angular factor corresponding to the orbital in question. Such calculations are straightforward when the relative orientations of the orbitals are well defined. However, given the complexities involved in assigning p-orbital orientations in B_{12} clusters, we have opted to not attempt these calculations at this time. That said, work is underway to address these issues using both theoretical and computational approaches.

*ENDOR field dependence [**1-3**]$^{1-}$*

Spectra collected mid field and at the high and low field edges are shown in Figure 4.15-4.17.

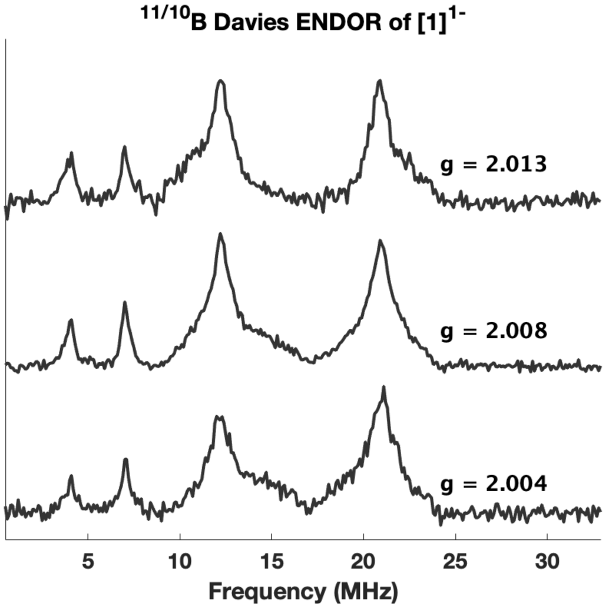

Figure 4.15. Field dependent Davies ENDOR spectra of [**1**]$^{1-}$ collected at 5 K and 34.11 GHz microwave frequency.

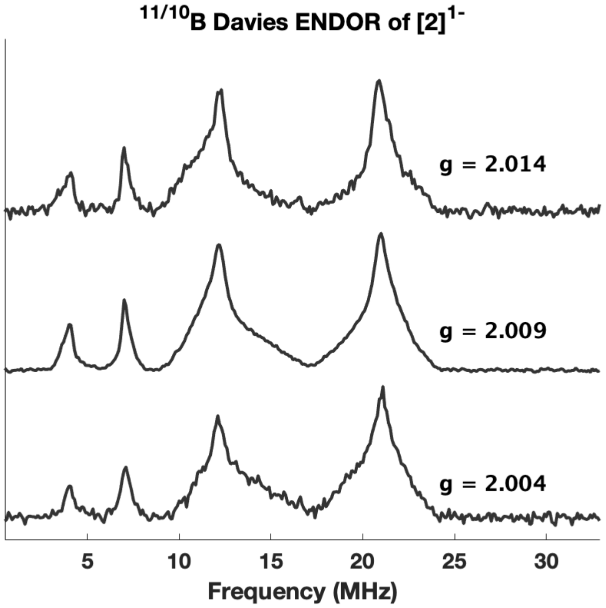

Figure 4.16. Field dependent Davies ENDOR spectra of [**2**]$^{1-}$ collected at 5 K and 34.12 GHz microwave frequency.

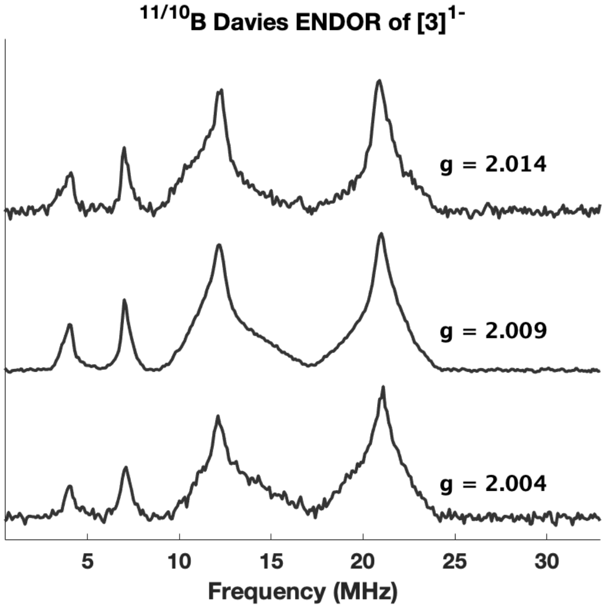

Figure 4.17. Field dependent Davies ENDOR spectra of [**3**]$^{1-}$ collected at 5 K and 34.11 GHz microwave frequency.

UV–vis–NIR Spectroscopy

All UV-vis-NIR Spectra were collected on a Varian Cary 500 UV-vis-NIR spectrometer in dual beam mode. Spectra were corrected for solvent backgrounds collected in 0% transmittance and 100% transmittance modes. Small-volume (~0.5 ml) quartz 1 cm path length cuvettes were used for high concentration NIR samples. Regular quartz 1 cm path length cuvettes were used to collect spectra in the UV-visible region. All spectra were collected in dichloromethane-d_2 (Cambridge Isotope Labs). The spectra did not change depending on if the samples were prepared air free (in a nitrogen-filled glove box) or open air.

BIBLIOGRAPHY

(1) Wixtrom, A. I.; Shao, Y.; Jung, D.; Machan, C. W.; Kevork, S. N.; Qian, E. A.; Axtell, J. C.; Khan, S. I.; Kubiak, C. P.; Spokoyny, A. M. Rapid Synthesis of Redox-Active Dodecaborane B12(OR)12 Clusters under Ambient Conditions. *Inorg. Chem. Front.* **2016**, *3* (5), 711–717. https://doi.org/10.1039/C5QI00263J.

(2) Messina, M. S.; Axtell, J. C.; Wang, Y.; Chong, P.; Wixtrom, A. I.; Kirlikovali, K. O.; Upton, B. M.; Hunter, B. M.; Shafaat, O. S.; Khan, S. I.; et al. Visible-Light-Induced Olefin Activation Using 3D Aromatic Boron-Rich Cluster Photooxidants. *J. Am. Chem. Soc.* **2016**, *138* (22), 6952–6955. https://doi.org/10.1021/jacs.6b03568.

(3) Longuet-Higgins, H. C.; Roberts, M. D. V. The Electronic Structure of an Icosahedron of Boron Atoms. *Proc R Soc Lond A* **1955**, *230* (1180), 110–119. https://doi.org/10.1098/rspa.1955.0115.

(4) Lipscomb, W. N. Recent Studies of the Boron Hydrides. In *Advances in Inorganic Chemistry and Radiochemistry*; Emeléus, H. J., Sharpe, A. G., Eds.; Academic Press, 1959; Vol. 1, pp 117–156. https://doi.org/10.1016/S0065-2792(08)60253-8.

(5) Wunderlich, J. A.; Lipscomb, W. N. STRUCTURE OF B12H12-2 ION. *J. Am. Chem. Soc.* **1960**, *82* (16), 4427–4428. https://doi.org/10.1021/ja01501a076.

(6) Lipscomb, W. N. The Boranes and Their Relatives. *Science* **1977**, *196* (4294), 1047–1055. https://doi.org/10.1126/science.196.4294.1047.

(7) Wiersema, R. J.; Middaugh, R. L. Electrochemical Preparation and Halogenation of 1,1'-.Mu.-Hydro-Bis(Undecahydro-Closo-Dodecaborate)(3-), B24H233-. *Inorg. Chem.* **1969**, *8* (10), 2074–2079. https://doi.org/10.1021/ic50080a009.

(8) Peymann, T.; Knobler, C. B.; Khan, S. I.; Hawthorne, M. F. Dodeca(Benzyloxy)Dodecaborane, B12(OCH2Ph)12: A Stable Derivative of Hypercloso-B12H12. *Angew. Chem. Int. Ed.* **2001**, *40* (9), 1664–1667. https://doi.org/10.1002/1521-3773(20010504)40:9<1664::AID-ANIE16640>3.0.CO;2-O.

(9) Axtell, J. C.; Messina, M. S.; Liu, J.-Y.; Galaktionova, D.; Schwan, J.; Porter, T. M.; Savage, M. D.; Wixtrom, A. I.; Rheingold, A. L.; Kubiak, C. P.; et al. Photooxidative Generation of Dodecaborate-Based Weakly Coordinating Anions. *Inorg. Chem.* **2019**, *58* (16), 10516–10526. https://doi.org/10.1021/acs.inorgchem.9b00935.

(10) Barton, J. L.; Wixtrom, A. I.; Kowalski, J. A.; Qian, E. A.; Jung, D.; Brushett, F. R.; Spokoyny, A. M. Perfunctionalized Dodecaborate Clusters as Stable Metal-Free Active Materials for Charge Storage. *ACS Appl. Energy Mater.* **2019**, *2* (7), 4907–4913. https://doi.org/10.1021/acsaem.9b00610.

(11) Aubry, T. J.; Axtell, J. C.; Basile, V. M.; Winchell, K. J.; Lindemuth, J. R.; Porter, T. M.; Liu, J.-Y.; Alexandrova, A. N.; Kubiak, C. P.; Tolbert, S. H.; et al. Dodecaborane-Based Dopants Designed to Shield Anion Electrostatics Lead to Increased Carrier Mobility in a Doped Conjugated Polymer. *Adv. Mater.* **2019**, *31* (11), 1805647. https://doi.org/10.1002/adma.201805647.

(12) Farha, O. K.; Julius, R. L.; Lee, M. W.; Huertas, R. E.; Knobler, C. B.; Hawthorne, M. F. Synthesis of Stable Dodecaalkoxy Derivatives of Hypercloso-B12H12. *J. Am. Chem. Soc.* **2005**, *127* (51), 18243–18251. https://doi.org/10.1021/ja0556373.

(13) Lee, M. W.; Farha, O. K.; Hawthorne, M. F.; Hansch, C. H. Alkoxy Derivatives of Dodecaborate: Discrete Nanomolecular Ions with Tunable Pseudometallic Properties. *Angew. Chem. Int. Ed.* **2007**, *46* (17), 3018–3022. https://doi.org/10.1002/anie.200605126.

(14) Peymann, T.; Knobler, C. B.; Hawthorne, M. F. An Unpaired Electron Incarcerated within an Icosahedral Borane Cage: Synthesis and Crystal Structure of the Blue, Air-Stable {[Closo-B12(CH3)12]·}– Radical. *Chem. Commun.* **1999**, *0* (20), 2039–2040. https://doi.org/10.1039/A905406E.

(15) Boeré, R. T.; Derendorf, J.; Jenne, C.; Kacprzak, S.; Keßler, M.; Riebau, R.; Riedel, S.; Roemmele, T. L.; Rühle, M.; Scherer, H.; et al. On the Oxidation of the Three-Dimensional Aromatics [B12X12]2− (X=F, Cl, Br, I). *Chem. – Eur. J.* **2014**, *20* (15), 4447–4459. https://doi.org/10.1002/chem.201304405.

(16) Boeré, R. T.; Kacprzak, S.; Keßler, M.; Knapp, C.; Riebau, R.; Riedel, S.; Roemmele, T. L.; Rühle, M.; Scherer, H.; Weber, S. Oxidation of Closo-[B12Cl12]2− to the Radical Anion [B12Cl12].− and to Neutral B12Cl12. *Angew. Chem. Int. Ed.* **2011**, *50* (2), 549–552. https://doi.org/10.1002/anie.201004755.

(17) Van, N.; Tiritiris, I.; Winter, R. F.; Sarkar, B.; Singh, P.; Duboc, C.; Muñoz-Castro, A.; Arratia-Pérez, R.; Kaim, W.; Schleid, T. Oxidative Perhydroxylation of [Closo-B12H12]2− to the Stable Inorganic Cluster Redox System [B12(OH)12]2−/.−: Experiment and Theory. *Chem. – Eur. J.* **2010**, *16* (37), 11242–11245. https://doi.org/10.1002/chem.201001374.

(18) Bambakidis, G.; Wagner, R. P. Electronic Structure and Binding Energy of the Icosahedral Boron Cluster B12†. *J. Phys. Chem. Solids* **1981**, *42* (11), 1023–1025. https://doi.org/10.1016/0022-3697(81)90068-8.

(19) Harris, D. C.; Bertolucci, M. D. *Symmetry and Spectroscopy: An Introduction to Vibrational and Electronic Spectroscopy*; New York: Oxford University Press, 1978.

(20) Mims, W. B. Pulsed Endor Experiments. *Proc. R. Soc. Lond. Ser. Math. Phys. Sci.* **1965**, *283* (1395), 452–457. https://doi.org/10.1098/rspa.1965.0034.

(21) Hyde, J. S.; Pasenkiewicz-Gierula, M.; Jesmanowicz, A.; Antholine, W. E. Pseudo Field Modulation in EPR Spectroscopy. *Appl. Magn. Reson.* **1990**, *1* (3), 483. https://doi.org/10.1007/BF03166028.

(22) Dikanov, S. A.; Tsvetkov, Y. Electron Spin Echo Envelope Modulation (ESEEM) Spectroscopy https://www.crcpress.com/Electron-Spin-Echo-Envelope-Modulation-ESEEM-Spectroscopy/Dikanov-Tsvetkov/p/book/9780849342240 (accessed Feb 27, 2020).

(23) Dikanov, S. A.; Xun, L.; Karpiel, A. B.; Tyryshkin, A. M.; Bowman, M. K. Orientationally-Selected Two-Dimensional ESEEM Spectroscopy of the Rieske-Type Iron−Sulfur Cluster in 2,4,5-Trichlorophenoxyacetate Monooxygenase from Burkholderia Cepacia AC1100. *J. Am. Chem. Soc.* **1996**, *118* (35), 8408–8416. https://doi.org/10.1021/ja960781x.

(24) Schweiger, A.; Jeschke, G. *Principles of Pulse Electron Paramagnetic Resonance*; Oxford University Press, 2001.

(25) Stoll, S.; Schweiger, A. EasySpin, a Comprehensive Software Package for Spectral Simulation and Analysis in EPR. *J. Magn. Reson.* **2006**, *178* (1), 42–55. https://doi.org/10.1016/j.jmr.2005.08.013.

(26) Tyryshkin, A. M.; Morton, J. J. L.; Ardavan, A.; Lyon, S. A. Davies Electron-Nuclear Double Resonance Revisited: Enhanced Sensitivity and Nuclear Spin Relaxation. *J. Chem. Phys.* **2006**, *124* (23), 234508. https://doi.org/10.1063/1.2204915.

(27) Buss, J. A.; Oyala, P. H.; Agapie, T. Terminal Molybdenum Phosphides with d Electrons: Radical Character Promotes Coupling Chemistry. *Angew. Chem. Int. Ed.* **2017**, *56* (46), 14502–14506. https://doi.org/10.1002/anie.201707921.

(28) Morton, J. R.; Preston, K. F. Atomic Parameters for Paramagnetic Resonance Data. *J. Magn. Reson. 1969* **1978**, *30* (3), 577–582. https://doi.org/10.1016/0022-2364(78)90284-6.